Available online at www.sciencedirect.com
SCIENCE DIRECT
International Journal of Heat and Mass Transfer 49 (2006) 4633–4652
International Journal of HEAT and MASS TRANSFER
www.elsevier.com/locate/ijhmt

Thermal hydraulics of the spallation target module of an accelerator driven sub-critical system: A numerical study

K. Arul Prakash [a], G. Biswas [a,*], B.V. Rathish Kumar [b]

[a] Department of Mechanical Engineering, Indian Institute of Technology, Kanpur 208 016, India
[b] Department of Mathematics, Indian Institute of Technology, Kanpur 208 016, India

Received 1 December 2005; received in revised form 17 April 2006
Available online 30 June 2006

Abstract

The mechanical design of the target module of an accelerator driven sub-critical nuclear reactor system (ADSS) calls for an analysis of the related thermal–hydraulic issues because of the sheer large amount of heat generation in its spallation target system during the course of nuclear interactions with the molten lead bismuth eutectic (LBE) target. The window of the target module is subject to high heat fluxes due to the direct impingement of high energy proton beam on its surface. A large amount of heat is deposited on the window and in the bulk of the LBE in the spallation region. Therefore, the problem of heat removal by the LBE is a challenging thermal–hydraulic issue. For this, one will need to examine the laminar/turbulent flows of low Prandtl number fluids (LBE) in a complex target module of an ADSS. In this study, the equations governing the flow and thermal energy are solved numerically using the streamline upwind Petrov–Galerkin (SUPG) finite element (FE) method. Special consideration has been given to the window under various thermal conditions, such as, isothermal, uniform and variable heat flux. The analysis has been extended to the case of heat generation in the liquid LBE. The principal purpose of the analysis is to trace the temperature distribution on the beam window and in the LBE. This also helps to check the suitability of the geometry in avoiding the recirculation or stagnation zones in the flow space that may lead to hot spots.

Keywords: ADSS; Spallation target; Finite element method; Streamline upwind Petrov–Galerkin technique; Heat flux; k–ϵ model

1. Introduction

In near future, ADSS will play a significant role as an alternative source of power generation. ADSS possesses a high potential for nuclear radioactive waste transmutation and operates in sub-critical conditions [1]. The target module of an ADSS is shown in Fig. 1. In the target system, a high energy proton beam from an accelerator irradiates a target, which is basically a flowing heavy density liquid metal (LBE). As a result, the liquid metal produces spallation neutrons that initiate a fission reaction in the sub-critical core. The target system of an ADSS has two sections: (1) the downcomer, incoming (2) the riser, outlet. The protons are induced on the target through a vacuum pipe closed by a window at the end. Therefore, the beam window is subject to high heat fluxes, thermal and mechanical stresses. A large amount of spallation heat is deposited on the window and in the LBE.

Though it is relatively easy to remove the total spallation heat by the LBE, it is crucial to achieve this without the target temperature exceeding the stipulated temperature in any region of the flow. There should not be any recirculation or stagnation zones leading to the hot spots, inadequate window cooling, generation of vapors, etc. This necessitates a detailed flow analysis in the spallation region, flow region near the entrance of the annular zone along with the determination of temperature distribution on the beam window.

The thermal–hydraulic behavior of a liquid–metal spallation region may be examined in either of the two ways:

* Corresponding author. Tel.: +91 0512 2597656; fax: +91 0512 2590534.
E-mail address: gtm@iitk.ac.in (G. Biswas).

0017-9310/$ - see front matter © 2006 Elsevier Ltd. All rights reserved.
doi:10.1016/j.ijheatmasstransfer.2006.04.018

Nomenclature

C_f	skin friction coefficient
C_p	coefficient of pressure
D	inlet hydraulic diameter
k_n	dimensionless turbulent kinetic energy $(=(k)/(V_0)^2)$
n_e	total number of elements
N_i, N_m	trial (also called shape/basis) functions
$[N]$	diagonal matrix, i.e. diag$[N_1, N_2, \ldots, N_{n_p}]$
Nu	Nusselt number
p	dimensionless pressure $(=(p)/(\rho)(V_0)^2)$
Re	Reynolds number
u, v	dimensionless velocity components in x and y directions $(=(u)/(V_0),(v)/(V_0))$
U^h	discontinuous streamline upwind contribution of weighting functions
W	admissible test function
$\overline{W}$	discontinuous test function for SUPG, ref. Eq. (25)
W^h	finite element approximation to test function W
$[W]$	diagonal matrix, i.e. diag$[W_1, W_2, \ldots, W_{n_p}]$
x, y	dimensionless cylindrical coordinate along radial and axial direction $(=(x)/(D),(y)/(D))$

Greek symbols

ϵ_n	dimensionless dissipation rate $(=(\epsilon)/(V_0)^3/(D))$
θ	dimensionless temperature $(=(T-T_\infty)/(T_w-T_\infty))$
$\nu_{t,n}$	dimensionless turbulent kinematic viscosity (ν_t/ν)
$\alpha_{t,n}$	dimensionless thermal diffusivity (α_t/α)
τ	dimensionless time $(t/(D/V_0))$; $t=$ dimensional time
ξ, η	normalized local coordinates
$\Re^2$	two-dimensional region
Γ_g, Γ_h	parts of Γ; ref. Eqs. (15) and (16)
σ_k	coefficients used in two (k–ϵ) equation turbulence model
σ_ϵ	coefficients used in two (k–ϵ) equation turbulence model
σ_t	coefficients used in wall treatment for energy equation
$\Delta\tau$	dimensionless time step
∇	Laplacian operator
$\otimes$	quantity following the symbol is independent of integrating variables

Subscript

∞	inlet condition

Superscripts

j	index for axisymmetry (=0 for planar and 1 for axisymmetric)
e	element
h	finite element approximation of a function
n	nth level time step
$*$	provisional values

The first option is to build a full-size target and install it in a proton beam, suitably supplied with coolant under design conditions and instrumented. The second is to simulate such a target using a state-of-the-art computational fluid dynamics (CFD) tool. Different geometric designs of LBE based ADSS are presently under consideration all over the world. The current status in the development of ADSS is presented by Maiorino et al. [2]. However, each of these models warrants a thorough investigation. Careful numerical experiments are needed to identify the flow stagnation and recirculation zones in the complex target system of an ADSS.

A review of the recent literature reveals that there have been few investigations focussing on the window region of an target system. Dury et al. [3] have analyzed the spallation zone near the beam window of the European Spallation source liquid–metal target facility numerically using CFX-4. They considered liquid mercury as the spallation target. Cho et al. [4] have computed the heat transfer and flow characteristics in a simplified version of the spallation zone of an axisymmetric target module called HYPER using ANSYS and CFX packages. While there is a circular flow guide in the target module considered by Dury et al. [3] there is no such flow guide in the model studied by Cho et al. [4]. Recently, window based ADSS models, such as, XADS [5] with funnel shaped flow guides have been proposed. In this model, the downcomer part of the target loop is separated from the riser part by using a flow guide. The flow takes a 180° turn around the tip of flow guide. Unlike in the earlier studies, in this case, it is essential to consider the entire target module of an ADSS rather than the riser part of the target system alone.

Therefore, in this paper we consider the entire target system with a straight flow guide (see Fig. 1). Further, we account for the high energetic proton beam impingement on the window surface by introducing a uniform and variable heat flux conditions on the window. In view of the continuous proton beam impingement, window surface may also be assumed to be isothermal for some situations. Also, we account for the heat generation in LBE based on FLUKA [6] data. The two equation k–ϵ model with the wall function approach is used for analyzing turbulent flows. An in-house SUPG-FEM code based on the

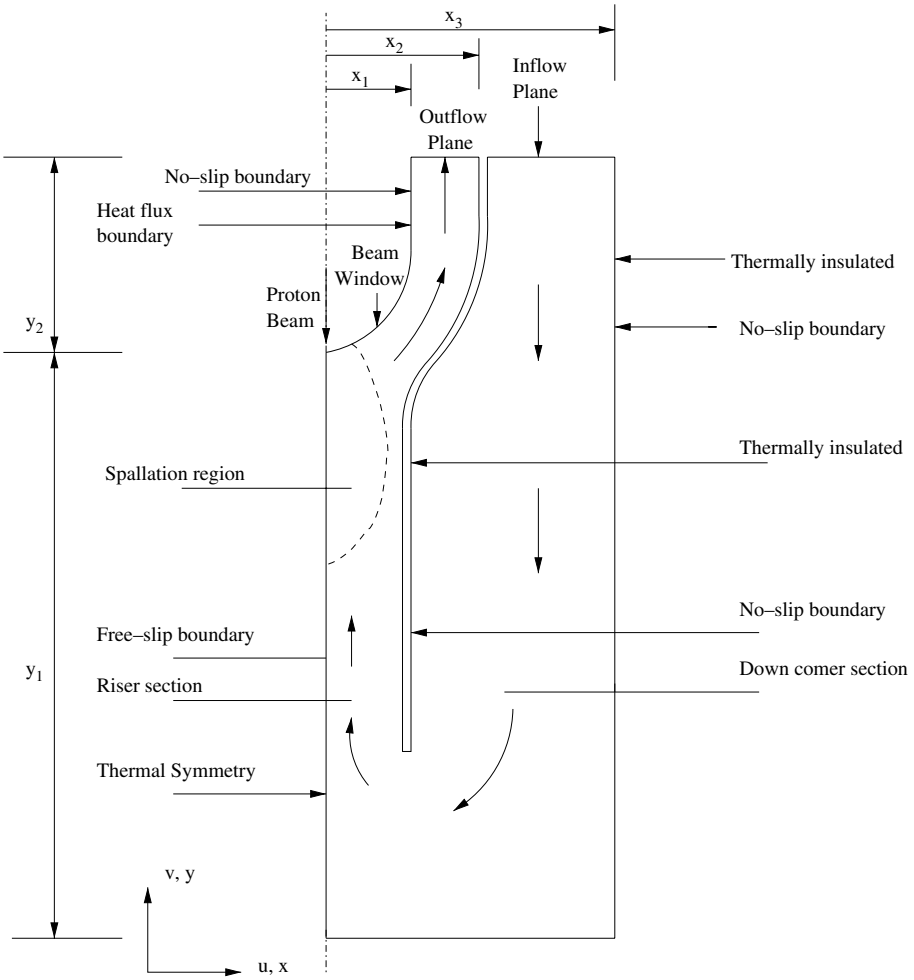

Fig. 1. Computational domain of the target module of an ADSS with boundary conditions.

projection scheme of Chorin [7] has been developed and validated. Simulations have been carried out to analyze the flow and heat transfer characteristics in the target module of an ADSS for a wide range of Reynolds numbers.

2. Governing equations and solution scheme

2.1. Governing equations

The flow is considered to be viscous, incompressible and turbulent. The geometry of interest is axisymmetric. The computational domain shown in Fig. 1 is discretized using small quadrilateral elements. All variables including the velocity components, pressure, temperature, kinetic energy and its dissipation rate are located at element nodes. The dimensionless equations governing the axisymmetric mean flow [8,9] are

Continuity equation

$$\frac{1}{x^j}\frac{\partial}{\partial x}(x^j u)+\frac{\partial v}{\partial y}=0 \tag{1}$$

Momentum equations

$$\frac{\partial u}{\partial \tau}+\left[u\frac{\partial u}{\partial x}+v\frac{\partial u}{\partial y}\right] = -\frac{\partial p}{\partial x}+\frac{1}{x^j}\frac{1}{Re}\left[\frac{\partial}{\partial x}\left(x^j v_{\text{eff}}\frac{\partial u}{\partial x}\right)+\frac{\partial}{\partial y}\left(x^j v_{\text{eff}}\frac{\partial u}{\partial y}\right)\right]+S_u \tag{2}$$

$$\frac{\partial v}{\partial \tau}+\left[u\frac{\partial v}{\partial x}+v\frac{\partial v}{\partial y}\right] = -\frac{\partial p}{\partial y}+\frac{1}{x^j}\frac{1}{Re}\left[\frac{\partial}{\partial x}\left(x^j v_{\text{eff}}\frac{\partial v}{\partial x}\right)+\frac{\partial}{\partial y}\left(x^j v_{\text{eff}}\frac{\partial v}{\partial y}\right)\right]+S_v \tag{3}$$

where

$$S_u=\frac{1}{x^j}\frac{1}{Re}\left[\frac{\partial}{\partial x}\left(x^j v_{\text{eff}}\frac{\partial u}{\partial x}\right)+\frac{\partial}{\partial y}\left(x^j v_{\text{eff}}\frac{\partial v}{\partial x}\right)-2j v_{\text{eff}}\frac{u}{x}\right] \tag{4}$$

$$S_v=\frac{1}{x^j}\frac{1}{Re}\left[\frac{\partial}{\partial x}\left(x^j v_{\text{eff}}\frac{\partial u}{\partial y}\right)+\frac{\partial}{\partial y}\left(x^j v_{\text{eff}}\frac{\partial v}{\partial y}\right)\right] \tag{5}$$

where p is the pressure and (u,v) are the radial and axial mean velocity components. Here, (x,y) the radial and axial coordinates, respectively. The equations describing two-dimensional plane flows can be obtained from Eqs. (1)–(5) by setting $j=0$. The effective turbulent viscosity $\nu_{\text{eff}} = (1+\nu_{\text{t},n})$ is calculated using the k–ϵ model of turbulence [10]

$$\nu_{\text{eff}} = 1 + c_\mu Re \frac{k_n^2}{\epsilon_n} \tag{6}$$

Transfer of the turbulent kinetic energy k_n, its dissipation rate ϵ_n and the temperature distribution θ are modeled as

k-equation

$$\frac{\partial k_n}{\partial \tau} + u\frac{\partial k_n}{\partial x} + v\frac{\partial k_n}{\partial y} = \frac{1}{x^j}\frac{1}{Re}\left[\frac{\partial}{\partial x}\left(x^j \frac{\nu_{\text{t},n}}{\sigma_k}\frac{\partial k_n}{\partial x}\right) + \frac{\partial}{\partial y}\left(x^j \frac{\nu_{\text{t},n}}{\sigma_k}\frac{\partial k_n}{\partial y}\right)\right] + G_n - \epsilon_n \tag{7}$$

ϵ-equation

$$\frac{\partial \epsilon_n}{\partial \tau} + u\frac{\partial \epsilon_n}{\partial x} + v\frac{\partial \epsilon_n}{\partial y} = \frac{1}{x^j}\frac{1}{Re}\left[\frac{\partial}{\partial x}\left(x^j \frac{\nu_{\text{t},n}}{\sigma_\epsilon}\frac{\partial \epsilon_n}{\partial x}\right) + \frac{\partial}{\partial y}\left(x^j \frac{\nu_{\text{t},n}}{\sigma_\epsilon}\frac{\partial \epsilon_n}{\partial y}\right)\right] + \frac{\epsilon_n}{k_n}(C_{1\epsilon}G_n - C_{2\epsilon}\epsilon_n) \tag{8}$$

Energy equation

$$\frac{\partial \theta}{\partial \tau} + u\frac{\partial \theta}{\partial x} + v\frac{\partial \theta}{\partial y} = \frac{1}{x^j}\frac{1}{RePr}\left[\frac{\partial}{\partial x}\left\{x^j(1+\alpha_{\text{t},n})\frac{\partial \theta}{\partial x}\right\} + \frac{\partial}{\partial y}\left\{x^j(1+\alpha_{\text{t},n})\frac{\partial \theta}{\partial y}\right\} + S_\theta\right] \tag{9}$$

where S_θ is the heat generation source term.

Production

$$G_n = \frac{\nu_{\text{t},n}}{Re}\left[2\left\{\left(\frac{\partial u}{\partial x}\right)^2 + \left(\frac{\partial v}{\partial y}\right)^2 + j\left(\frac{u}{x}\right)^2\right\} + \left(\frac{\partial u}{\partial y} + \frac{\partial v}{\partial x}\right)^2\right] \tag{10}$$

where G_n is the production term. Finally, $\nu_{\text{t},n}$ and $\alpha_{\text{t},n}$ can be written as

$$\nu_{\text{t},n} = C_\mu Re \frac{k_n^2}{\epsilon_n}; \quad \alpha_{\text{t},n} = C_\mu Re \frac{Prk_n^2}{\sigma_{\text{t}}\epsilon_n} \tag{11}$$

Also, $C_\mu = 0.09$, $\sigma_k = 1.0$, $\sigma_\epsilon = 1.3$, $\sigma_{\text{t}} = 0.9$, $C_{1\epsilon} = 1.44$, $C_{2\epsilon} = 1.92$

$$\text{Reynolds number } (Re) = \frac{V_0 D}{\nu}; \quad \text{Prandtl number } (Pr) = \frac{\nu}{\alpha}$$

where D is the characteristic length, ν the kinematic viscosity, α the thermal diffusivity and V_0 is the mean inlet velocity.

2.2. Solution scheme

2.2.1. Eulerian velocity correction approach

This method is essentially based on the projection scheme of Chorin [7], which was originally developed in a finite difference context and identical to the Marker and Cell (MAC) method of Harlow and Welch [11]. This has been extended to two-dimensional finite element method by Donea et al. [12], Ramaswamy et al. [13] and du Toit [14]. In the present study, the algorithm has been applied to the axi-symmetric solution of turbulent flow. The solution for each time step is obtained through following four steps.

Step 1: Calculation of provisional velocities. The provisional velocities are calculated from the momentum equations by dropping the pressure terms. Since these explicitly advanced velocities do not necessarily satisfy the continuity equation, they are called as provisional velocities and shown starred. For instance, the radial component of velocity can be written as

$$u^* = u^n + \Delta\tau\left[-\frac{3}{2}\left(u\frac{\partial u}{\partial x} + v\frac{\partial u}{\partial y}\right)^n + \frac{1}{2}\left(u\frac{\partial u}{\partial x} + v\frac{\partial u}{\partial y}\right)^{n-1}\right] + \Delta\tau\left[\frac{1}{x^j}\frac{1}{Re}\left[\frac{\partial}{\partial x}\left\{x^j\mu_{\text{e}}\frac{\partial u}{\partial x}\right\} + \frac{\partial}{\partial y}\left\{x^j\mu_{\text{e}}\frac{\partial u}{\partial y}\right\}\right] + S_u\right]^n$$

Step 2: Solution of pressure equation. The pressure term, which was initially ignored may be taken into account now. Thus we obtain

$$u^{n+1} = u^* - \Delta\tau\left[\frac{\partial p}{\partial x}\right]^{n+1}; \quad v^{n+1} = v^* - \Delta\tau\left[\frac{\partial p}{\partial y}\right]^{n+1} \tag{12}$$

Taking the divergence of Eq. (12) and imposing the condition $(\nabla \cdot V)^{n+1} = 0$, we get the Poisson equation

$$[\nabla^2 p]^{n+1} = \frac{1}{\Delta\tau}(\nabla \cdot V^*) \tag{13}$$

the right hand side (RHS) of which can be computed from the provisional velocities. The Poisson equation is then solved using incomplete Cholesky preconditioned conjugate residual method with proper boundary conditions to obtain the pressure at the $(n+1)$ time step.

Step 3: Velocity correction. The velocities are corrected at the next time step by updating the provisional velocities using the evaluated pressure. Eq. (12) is used to calculate the velocities u^{n+1} and v^{n+1}. One can interpret the role of pressure in an incompressible flow as a projection operator which projects an arbitrary vector field into a divergence free vector field.

Step 4: Calculation of turbulent kinetic energy and its dissipation rate. Solve the turbulent kinetic energy (k_n) Eq. (7) and the dissipation (ϵ_n) Eq. (8) to calculate

turbulent viscosity ($\nu_{t,n}$) and turbulent diffusivity ($\alpha_{t,n}$) using Eq. (11). A steady solution is obtained through pseudo time marching. Finally, the energy Eq. (9) is solved with the steady state velocity field.

3. Formulation

Eqs. (2) and (3) without the pressure term and Eqs. (7)–(9) may be represented as a single equation shown below:

$$\frac{\partial\phi}{\partial\tau}+u\frac{\partial\phi}{\partial x}+v\frac{\partial\phi}{\partial y} = S_\phi+\frac{1}{x_j}\left[\frac{\partial}{\partial x}\left(x^j\Gamma_\phi\frac{\partial\phi}{\partial x}\right)+\frac{\partial}{\partial y}\left(x^j\Gamma_\phi\frac{\partial\phi}{\partial y}\right)\right] \tag{14}$$

Let Ω (geometry of interest) be a bounded region in $\Re^2$ bounded by the piecewise smooth boundary Γ. Let $\mathbf{x}=\{x,y\}$ denote the vector of spatial coordinate of a generic point in $\overline{\Omega}$ and let τ denote the time value in the interval $I=[0,T]$. Also consider $\vec{n}$ as the outward normal vector to Γ and Γ_g, Γ_h as sections of Γ which satisfy the following

$$\overline{\Gamma_g\bigcup\Gamma_h}=\Gamma \tag{15}$$

$$\Gamma_g\bigcap\Gamma_h=\emptyset \tag{16}$$

The superimposed bar in Eq. (15) represents set closure and $\emptyset$ in Eq. (16) denotes the empty set. Now our focus is on the finite element formulation of the problem defined by Eqs. (12)–(14). The formulation is also presented in Maji and Biswas [15].

3.1. Finite element formulation

In order to find a discrete solution of Eqs. (12)–(14), we assume Ω is discretized in n_e quadrilateral elements such that

$$\bigcup_{e=1}^{n_e}\overline{\Omega^e}=\overline{\Omega}\quad\bigcap_{e=1}^{n_e}\Omega^e=\emptyset \tag{17}$$

where Ω^e denotes the interior domain of an element. Let Γ^e be boundary of Ω^e. Finally, the 'interior boundary' Γ_{int} is defined as the following

$$\Gamma_{\text{int}}=\bigcup_{e=1}^{n_e}\Gamma^e-\Gamma \tag{18}$$

Let (ϕ^h,p^h) be an element of S^h and W^h be an element of V^h, where S^h and V^h are finite dimensional sub-spaces of the trial (S) and test (V) spaces respectively and are defined as

$$S^h=\{(\Phi^h)\in(C^0(\Omega))^6,\ \Phi^h=g_\phi \text{ and } p^h=s \text{ on } \Gamma_g^*\}$$

$$V^h=\{W^h\in C^0(\Omega),\ W^h=0 \text{ on } \Gamma_g^*\}$$

We assume that this $C^0(\Omega)$ functions are typical finite element shape (trial) functions of Lagrange type which will also belong to $H^1(\Omega)$ functional space. Now finite element method can be formulated by requiring the discrete solution ϕ^h, p^h to satisfy the weak form of Eqs. (12)–(14).

Thus Eq. (14) becomes

$$\int_\Omega W^h\left[\frac{\partial\phi^h}{\partial\tau}+u^h\frac{\partial\phi^h}{\partial x}+v^h\frac{\partial\phi^h}{\partial y}\right]d\Omega+\int_\Omega\Gamma_\phi\left[\frac{\partial W^h}{\partial x}\frac{\partial\phi^h}{\partial x}+\frac{\partial W^h}{\partial y}\frac{\partial\phi^h}{\partial y}\right]d\Omega-\int_{\Gamma_h}\Gamma_\phi W^h h_\phi\,d\Gamma=\int_\Omega W^h S_\phi\,d\Omega \tag{19}$$

In a similar manner, Eq. (12) becomes

$$\int_\Omega W^h\frac{\partial u^h}{\partial\tau}d\Omega=\int_\Omega W^h\frac{\partial(u^h)^*}{\partial\tau}d\Omega-\int_\Omega W^h\frac{\partial p^h}{\partial x}d\Omega$$

$$\int_\Omega W^h\frac{\partial v^h}{\partial\tau}d\Omega=\int_\Omega W^h\frac{\partial(v^h)^*}{\partial\tau}d\Omega-\int_\Omega W^h\frac{\partial p^h}{\partial y}d\Omega \tag{20}$$

Following a similar approach, Eq. (13) becomes

$$\int_\Omega\left[\frac{\partial W^h}{\partial x}\frac{\partial p^h}{\partial x}+\frac{\partial W^h}{\partial y}\frac{\partial p^h}{\partial y}\right]d\Omega=-\frac{1}{\Delta\tau}\int_\Omega W^h\left[\frac{1}{x^j}\frac{\partial}{\partial x}\{x^j(u^h)^*\}+\frac{\partial}{\partial y}(v^h)^*\right]d\Omega+\int_{\Gamma_g}W^h b\,d\Gamma \tag{21}$$

Let the finite set $\{N_i\}$ represent a basis for S^h, while $\{W_i\}$ be the basis for V^h. The function N_i, W_i are associated with the node i of the finite element mesh. The discrete solution ϕ^h, p^h and Γ_ϕ^h can be approximated within each element as a linear combination of the trial (basis) function. The expression for ϕ^h is given as

$$\phi^h=\sum_{m=1}^{N_p}\{\phi(\tau)\}_m N_m=\{N\}^{\mathrm{T}}\{\phi(\tau)\} \tag{22}$$

where N_p is the total number of nodes in each element and $\{N\}$ represents a column matrix of dimension $1\times N_p$ and $\{N\}^{\mathrm{T}}$ represents transpose of $\{N\}$. The curly brackets $\{\ \}$ enclosing some quantity indicate that the corresponding nodal quantities are arranged node-wise in a column vector form. The trial functions $\{N\}$ are piecewise bilinear. Similarly the expressions are written for p^h and Γ_ϕ^h.

The four noded bilinear elements are mapped on a 2×2 square using isoparametric transformation. The test functions and trial functions for the velocity correction (20) and pressure Poisson equation (21) are same in this formulation. However for Eq. (19) formulation will be different which will be explained in the next section. Following the mass lumping concept the final form of Eqs. (20) and (21) are as follows:

- *Velocity correction equations*

$$\sum_{e=1}^{n_e}\int_{\Omega^e}[N]\,d\Omega\otimes\{u^{n+1}\}=\sum_{e=1}^{n_e}\int_{\Omega^e}[N]\,d\Omega\otimes\{u^*\}-\Delta\tau\sum_{e=1}^{n_e}\int_{\Omega^e}\{N\}\,d\Omega\otimes\frac{\partial p^{n+1}}{\partial x}$$

$$\sum_{e=1}^{n_e}\int_{\Omega^e}[N]\,d\Omega\otimes\{v^{n+1}\}=\sum_{e=1}^{n_e}\int_{\Omega^e}[N]\,d\Omega\otimes\{v^*\}-\Delta\tau\sum_{e=1}^{n_e}\int_{\Omega^e}\{N\}\,d\Omega\otimes\frac{\partial p^{n+1}}{\partial y} \tag{23}$$

- *Pressure Poisson equation*

$$\sum_{e=1}^{n_e}\int_{\Omega^e}\left[\left\{\frac{\partial N}{\partial x}\right\}\left\{\frac{\partial N}{\partial x}\right\}^{\mathrm{T}}+\left\{\frac{\partial N}{\partial y}\right\}\left\{\frac{\partial N}{\partial y}\right\}^{\mathrm{T}}\right]d\Omega\otimes\{p^{n+1}\}=-\frac{1}{\Delta\tau}\sum_{e=1}^{n_e}\int_{\Omega^e}\{N\}\left[\left\{\frac{\partial N}{\partial x}\right\}^{\mathrm{T}}\{u^*\}+\left\{\frac{\partial N}{\partial y}\right\}^{\mathrm{T}}\{v^*\}+\frac{\{N\}^{\mathrm{T}}\{u^*\}}{\{N\}^{\mathrm{T}}\{x\}}\right]d\Omega+\sum_{l}\int_{\Gamma_g^l}\{N\}b\,d\Gamma \tag{24}$$

3.2. Streamline upwind Petrov–Galerkin (SUPG) based formulation

The numerical scheme based on standard Galerkin (Bubnov–Galerkin) finite element method for convection–diffusion problems produces non-physical oscillatory solution when convection dominates over diffusion. To overcome this cross-wind problem, Brooks and Hughes [16] introduced streamline upwind Petrov–Galerkin (SUPG) technique with the application of modified weighting functions for all terms of the governing equations given by

$$\overline{W}^h=W^h+U^h \tag{25}$$

where W^h is a continuous weighting function and U^h is the discontinuous streamline upwind contribution. Both W^h and U^h are assumed to be smooth on the element interiors. The above discontinuous test functions U^h introduce a corrective diffusion which is highly anisotropic with a non-zero coefficient only in the direction of the resultant element velocity vector calculated at the geometric center of the element. This is to make this term active only in the direction of the resultant element velocity and thereby effectively introduces upwinding in multi-dimensional problem. It is to be noted that in the SUPG formulation, U^h weights only on the element interiors. Also, the element coefficient matrix is mass lumped. Incorporating all these concepts, the Eq. (19) may be rewritten as

$$\begin{aligned}\sum_{e=1}^{n_e}\int_{\Omega^e}[\overline{W}]\,d\Omega\otimes\left\{\frac{\phi^*-\phi^n}{\Delta\tau}\right\}&\approx-\sum_{e=1}^{n_e}\int_{\Omega^e}\{\overline{W}\}\left[\{N\}^{\mathrm{T}}\{u^n\}\left\{\frac{\partial N}{\partial x}\right\}^{\mathrm{T}}\{\phi^n\}+\{N\}^{\mathrm{T}}\{v^n\}\left\{\frac{\partial N}{\partial y}\right\}^{\mathrm{T}}\{\phi^n\}\right]d\Omega\\&+\sum_{l}\int_{\Gamma_h^l}\{W\}\Gamma_\phi^h h_\phi\,d\Gamma-\sum_{e=1}^{n_e}\int_{\Omega^e}\Gamma_\phi^h\left[\left\{\frac{\partial W}{\partial x}\right\}\left\{\frac{\partial N}{\partial x}\right\}^{\mathrm{T}}\{\phi^n\}+\left\{\frac{\partial W}{\partial y}\right\}\left\{\frac{\partial N}{\partial y}\right\}^{\mathrm{T}}\{\phi^n\}\right]d\Omega+\sum_{e=1}^{n_e}\int_{\Omega^e}\{\overline{W}\}S_\phi^h\,d\Omega\\&+\sum_{e=1}^{n_e}\int_{\Omega^e}\{U\}\left[\frac{\partial\Gamma_\phi^h}{\partial x}\left\{\frac{\partial N}{\partial x}\right\}^{\mathrm{T}}\{\phi^n\}+\frac{\partial\Gamma_\phi^h}{\partial y}\left\{\frac{\partial N}{\partial y}\right\}^{\mathrm{T}}\{\phi^n\}+\Gamma_\phi^h j\left\{\frac{\partial N}{\partial x}\right\}^{\mathrm{T}}\left\{\frac{\phi^n}{x}\right\}\right]d\Omega\end{aligned} \tag{26}$$

which allows us to compute the provisional value ϕ at the new time step in terms of the quantities at the previous time step value.

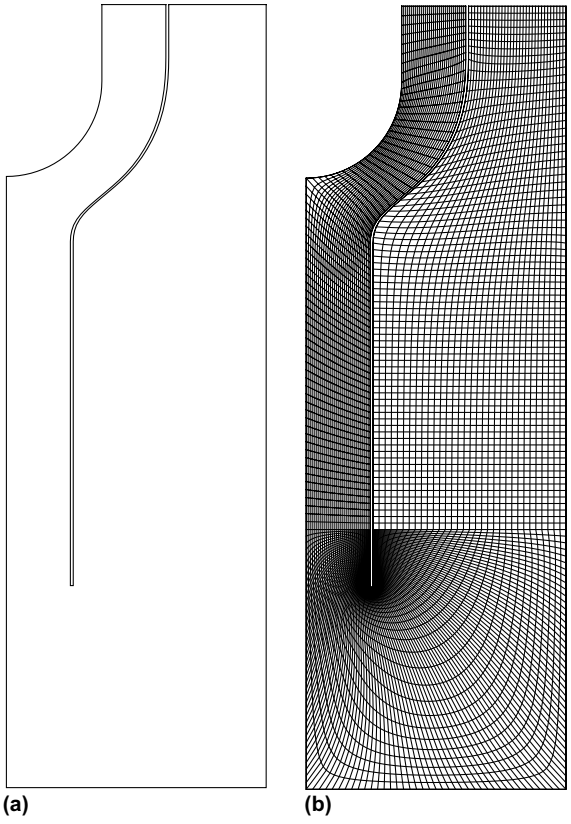

Fig. 2. (a) Outer domain, (b) computational grid.

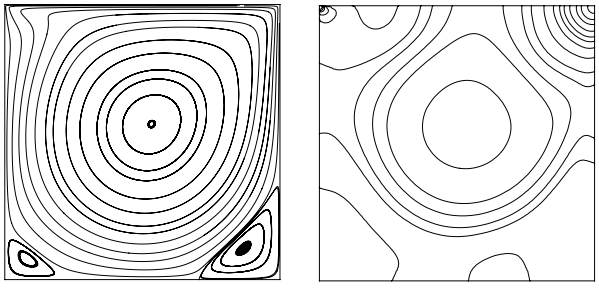

Fig. 3. Streamlines and pressure contours −0.06(0.02)0.1 of lid-driven cavity flow for $Re = 1000$ (129×129 grid).

4. Boundary conditions

4.1. Laminar flow

The boundary conditions of interest in this investigation are

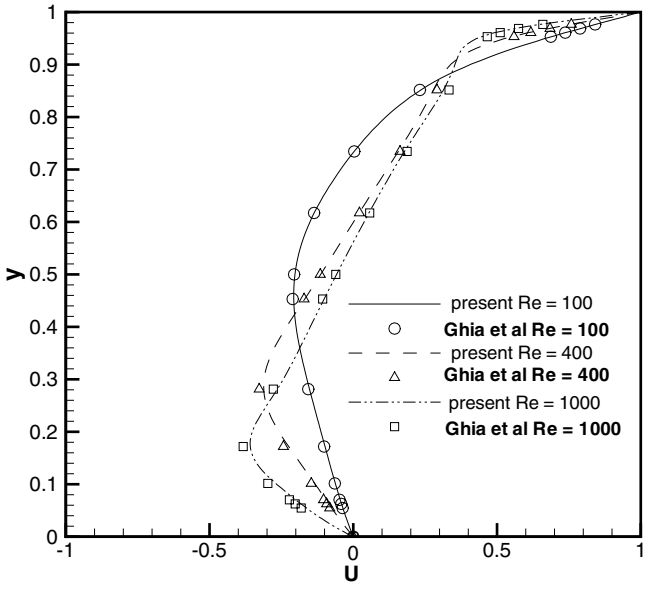

Fig. 4. Comparison of u velocity along vertical centre line with Ghia et al. for lid-driven cavity flow.

- Inlet section:

$$u = 0, \quad v = v(x); \quad \theta = 0$$

- Symmetry wall:

$$u = 0, \quad \frac{\partial v}{\partial n} = 0; \quad \frac{\partial \theta}{\partial n} = 0$$

- No slip wall:

$$u = v = 0$$

For temperature, along the beam window

1. $\theta = 1.0$ (constant temperature);
2. $\theta = \dfrac{W_2 - W_i}{W_2 - W_1}$ (variable temperature);
3. $\dfrac{\partial \theta}{\partial n} = 1.0$ (constant heat flux);
4. $\dfrac{\partial \theta}{\partial n} = \dfrac{W_2 - W_i}{W_2 - W_1}$ (variable heat flux);

where,
W_i = Local non-dimensional length from the leading edge of the window.
W_1 and W_2 = Non-dimensional distance at the leading and trailing edge of the beam window.
n is the normal direction.

For other walls $\dfrac{\partial \theta}{\partial n} = 0$ (thermally insulated)

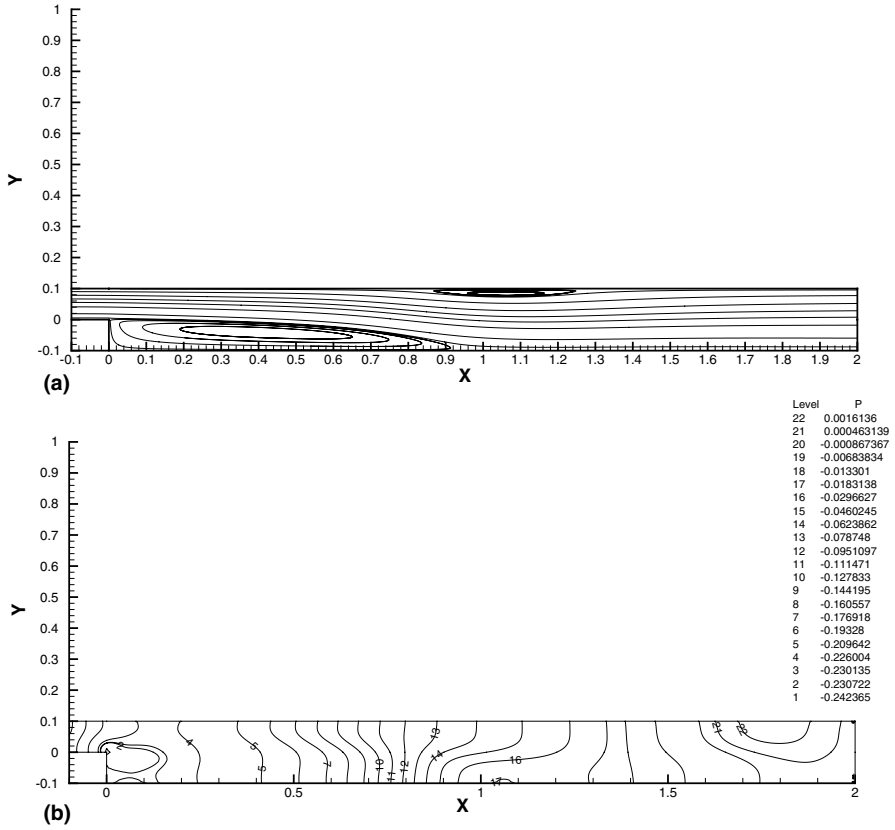

Fig. 5. Two-dimensional backward-facing step problem: (a) streamline plot, (b) pressure contours for $Re = 500$.

- Outlet section:

$$\frac{\partial u}{\partial n} = \frac{\partial v}{\partial n} = 0; \quad \frac{\partial \theta}{\partial n} = 0$$

Non-dimensionalization of energy equation for the case of flux boundary condition is done with respect to dimensional heat flux at the window. However the final form of the energy equation remains the same.

4.2. Turbulent flow

The standard k–ϵ turbulence model, which relies on the high-Reynolds number assumption, is not valid very near to the wall where the viscous effects are predominant. The wall function approach has been followed to model the near wall region [17]. In this approach the flow near the solid boundaries is not solved for but is assumed to obey the *law of the wall*. The tangential velocity and the turbulence quantities are then specified. The estimation of wall shear stress based on the finite element method is adopted using Benim and Zinser [18]. The conditions for velocity and temperature can be specified in the following way:

- Inlet plane:

$$\begin{aligned} &v = v(x); \quad u = 0 \\ &k_n = 1.5I^2; \quad \epsilon_n(x) = \left(k_n^{3/2} C_\mu^{3/4}\right) \Big/ \chi x \quad \text{for } x < (\lambda/\chi) \\ &\qquad\qquad = \left(k_n^{3/2} C_\mu^{3/4}\right) \Big/ \lambda x_p \quad \text{for } x > (\lambda/\chi) \\ &\theta = 0 \end{aligned} \tag{27}$$

where $v_{\tau,n}$ is non-dimensional friction velocity, x^+ is given by xv_τ/v, I is the turbulent intensity, $\chi = 0.42$ which is known as Von Karman constant, λ is a constant prescribing ramp distribution of mixing length in boundary layers and equal to 0.09 and $E = 9.743$. The boundary conditions at the outlet and the confining walls are given as the following [19]:

- Symmetry wall:

$$u = 0, \quad \frac{\partial f}{\partial n} = 0; \quad f = (v, \theta, k_n, \epsilon_n)$$

- Outlet section:

$$\frac{\partial f}{\partial n} = 0; \quad f = (u, v, \theta, k_n, \epsilon_n)$$

The wall functions due to Launder and Spalding [17] are used to mimic the near wall region for the no slip walls. For, $x_p^+ \geqslant 11.63$

$$\tau_{w,n}^{v} = \frac{v_p C_\mu^{1/4} k_{n,p}^{1/2} \chi}{\ln(E x_p^+)} \tag{28}$$

where $x_p^+ = x_p Re\, C_\mu^{1/4} k_{n,p}^{1/2}$. The subscript p refers to the first grid point adjacent to the wall.

Instead of using Eqs. (7) and (8) near the wall, k_n, ϵ_n at point p are computed from

$$k_{n,p} = \frac{v_{\tau,n}^2}{C_\mu^{1/2}}; \quad \epsilon_{n,p} = \frac{v_{\tau,n}^3}{\chi x_p} \tag{29}$$

where, $v_{\tau,n}$ is the non-dimensional friction velocity.

5. Grid generation and code validation

The computational grid is generated using algebraic method, smoothened and clustered by elliptic partial

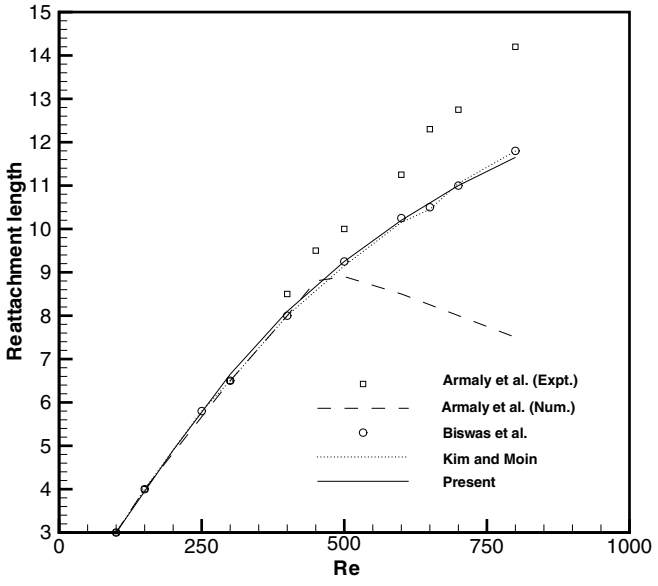

Fig. 6. Re-attachment length versus Reynolds number for the backward facing step.

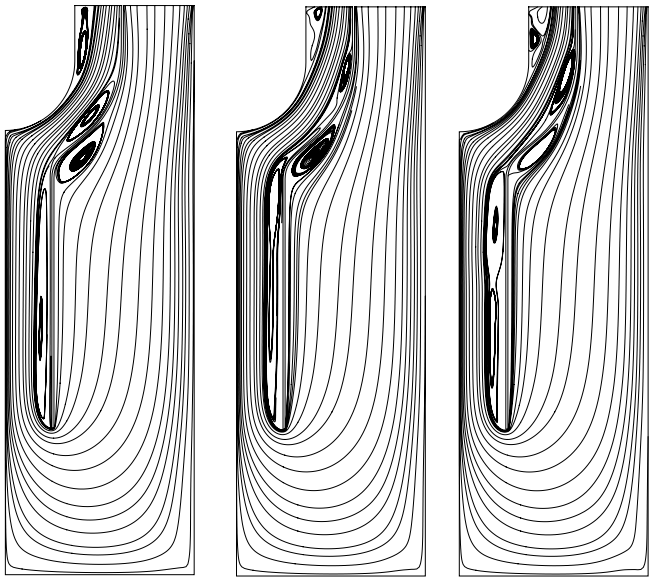

Fig. 7. Streamlines for (i) $Re = 500$, (ii) $Re = 700$ and (iii) $Re = 1000$.

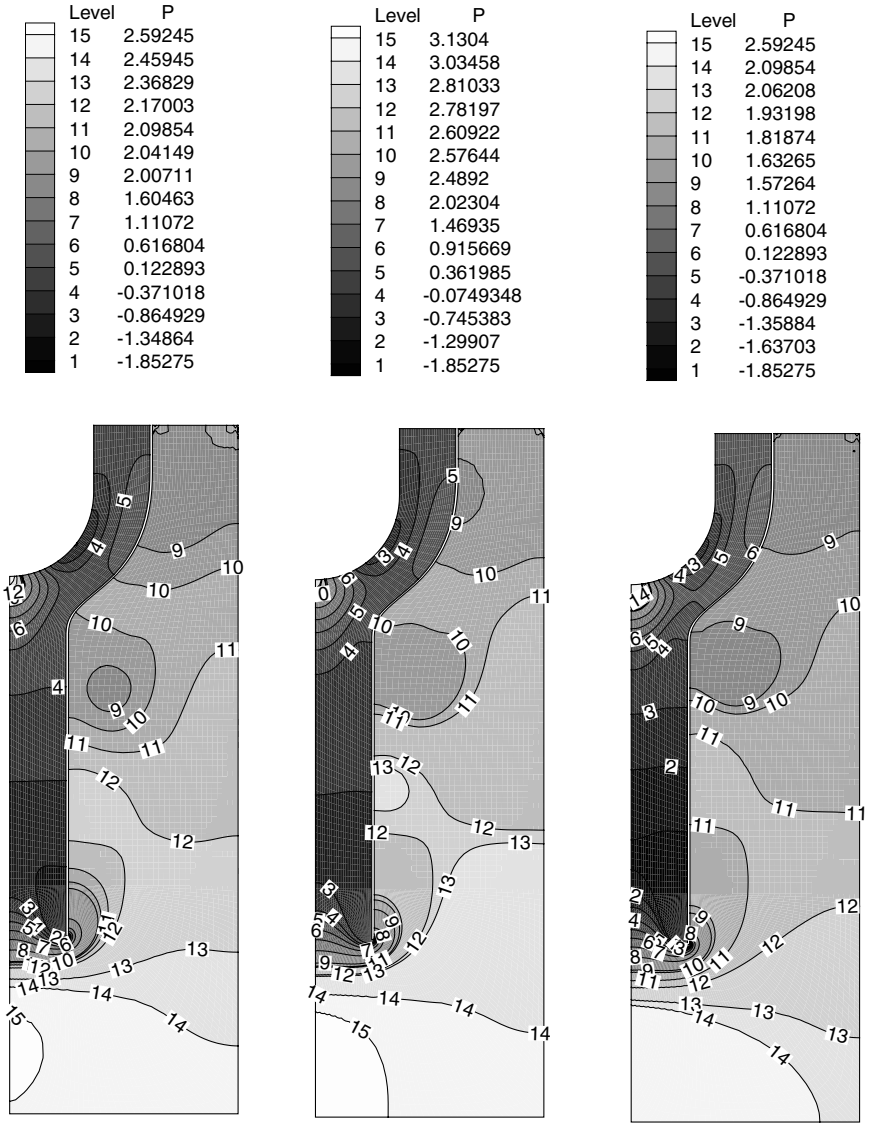

Fig. 8. Pressure contours for (i) $Re = 500$, (ii) $Re = 700$ and (iii) $Re = 1000$.

grid generation technique using Poisson's equations. The outer domain and the computational grid is shown in Fig. 2.

In order to validate our inhouse SUPG-FE code, it is tested on two benchmark problems, namely the flow in a lid-driven cavity, the flow over a backward-facing step. Our grid-independent results for these problems are compared with those available in the literature.

5.1. Lid driven cavity

A Lid driven cavity flow is the most commonly used computational experiment to demonstrate the performance of an incompressible Navier–Stokes solver. A comprehensive collection of results for different Reynolds number has been presented by Ghia et al. [20]. The boundary conditions have been taken same as in [20]. The streamlines and pressure contours are shown in Fig. 3. The u velocity profile along the vertical centerline of the cavity is compared with the benchmark solutions of Ghia et al. [20] for $Re = 100$, 400 and 1000. The results are in good agreement with the benchmark solution (see Fig. 4).

5.2. Backward-facing step flow

The Backward-facing step is considered for varying Reynolds number to verify the stability and accuracy of the proposed methods when analyzing an inflow–outflow problem. The H/h expansion ratio has been taken as 1.9423 (same as Armaly et al. [21]). The streamlines and pressure contours for $Re = 500$ are shown in Fig. 5. The variation of reattachment length is compared with the experimental and numerical results of Armaly et al. [21] and numerical results of Kim and Moin [22] and Biswas et al. [23]. The results are found to be in nice agreement with the experimental and numerical data which is shown in Fig. 6. The computational results start deviating from

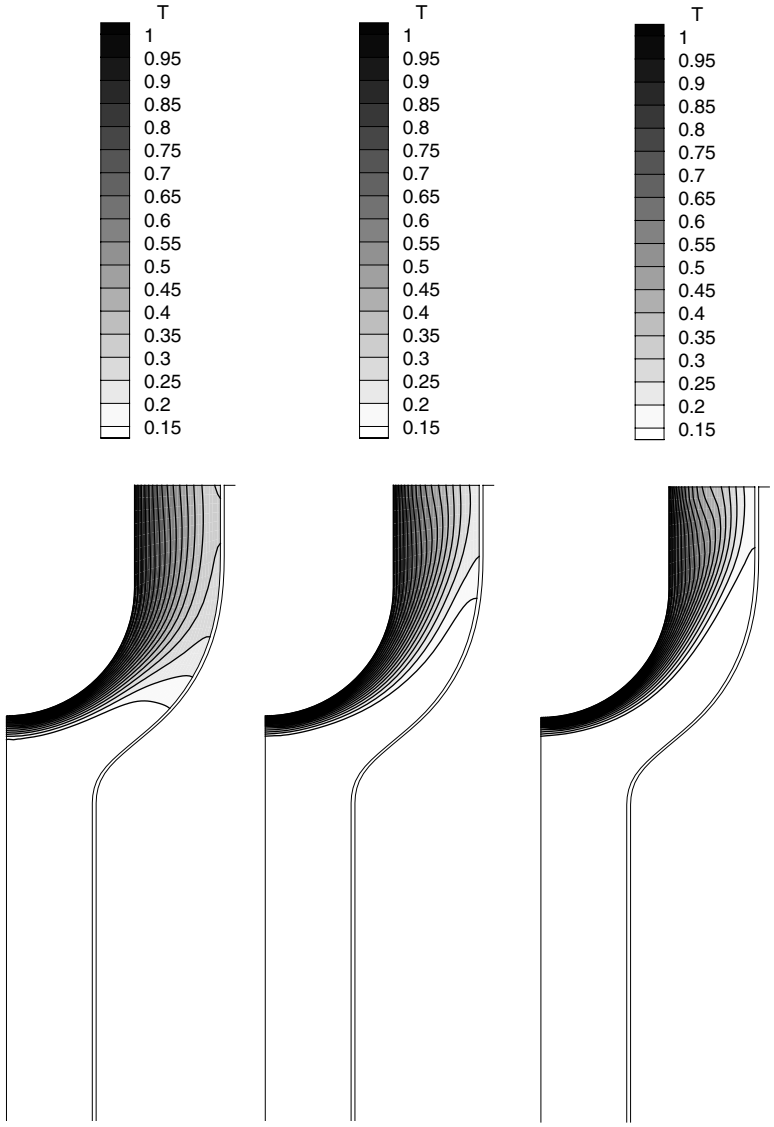

Fig. 9. Constant temperature contours (magnified view of the window section) for (i) $Re = 500$, (ii) $Re = 700$ and (iii) $Re = 1000$.

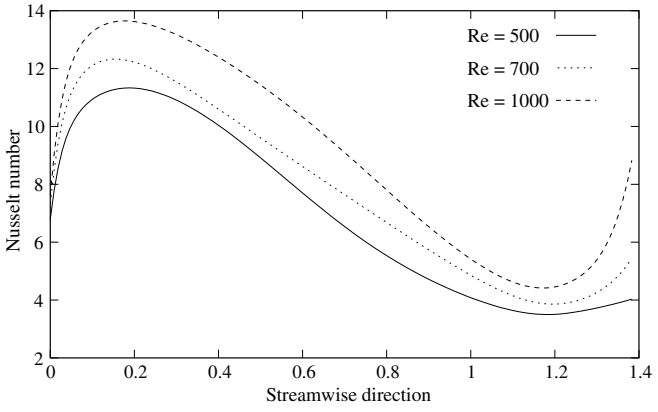

Fig. 10. Nusselt number for constant temperature (i) $Re = 500$, (ii) $Re = 700$ and (iii) $Re = 1000$.

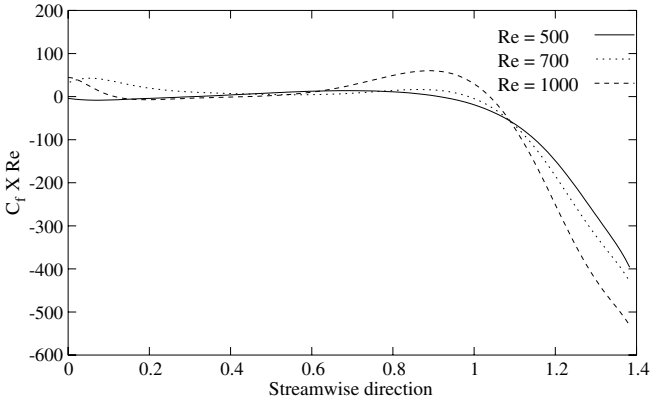

Fig. 11. Skin friction coefficient for (i) $Re = 500$, (ii) $Re = 700$ and (iii) $Re = 1000$.

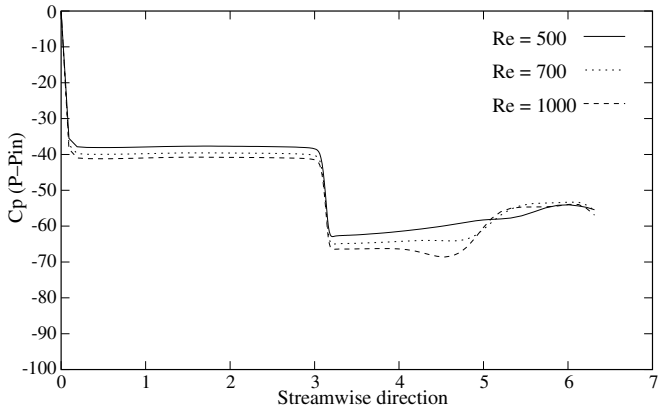

Fig. 12. Coefficient of pressure for (i) $Re = 500$, (ii) $Re = 700$ and (iii) $Re = 1000$.

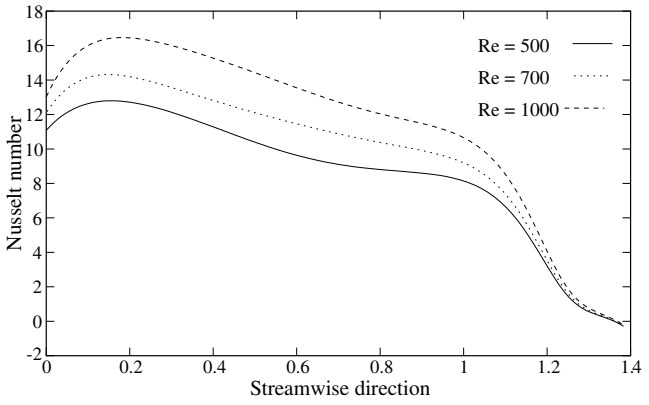

Fig. 14. Nusselt number for variable temperature (i) $Re = 500$, (ii) $Re = 700$ and (iii) $Re = 1000$.

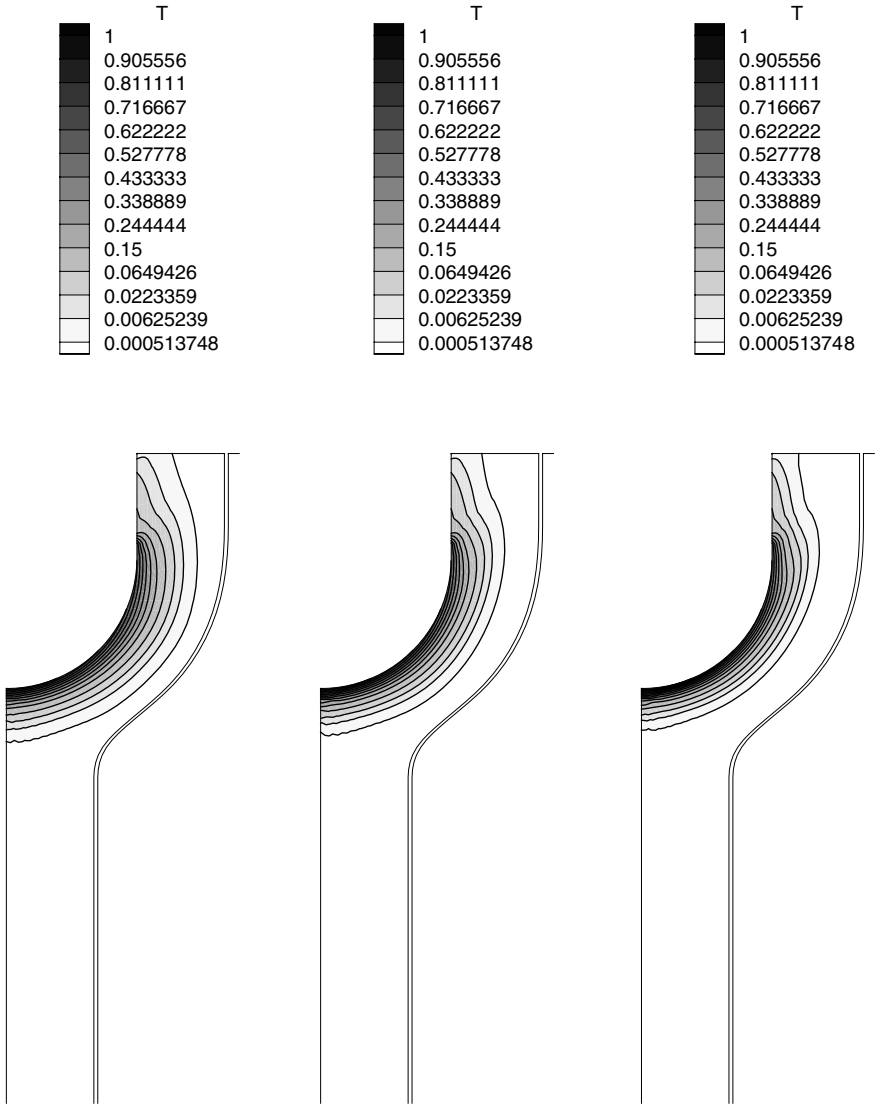

Fig. 13. Variable temperature contours (magnified view of the window section) for (i) $Re = 500$, (ii) $Re = 700$ and (iii) $Re = 1000$.

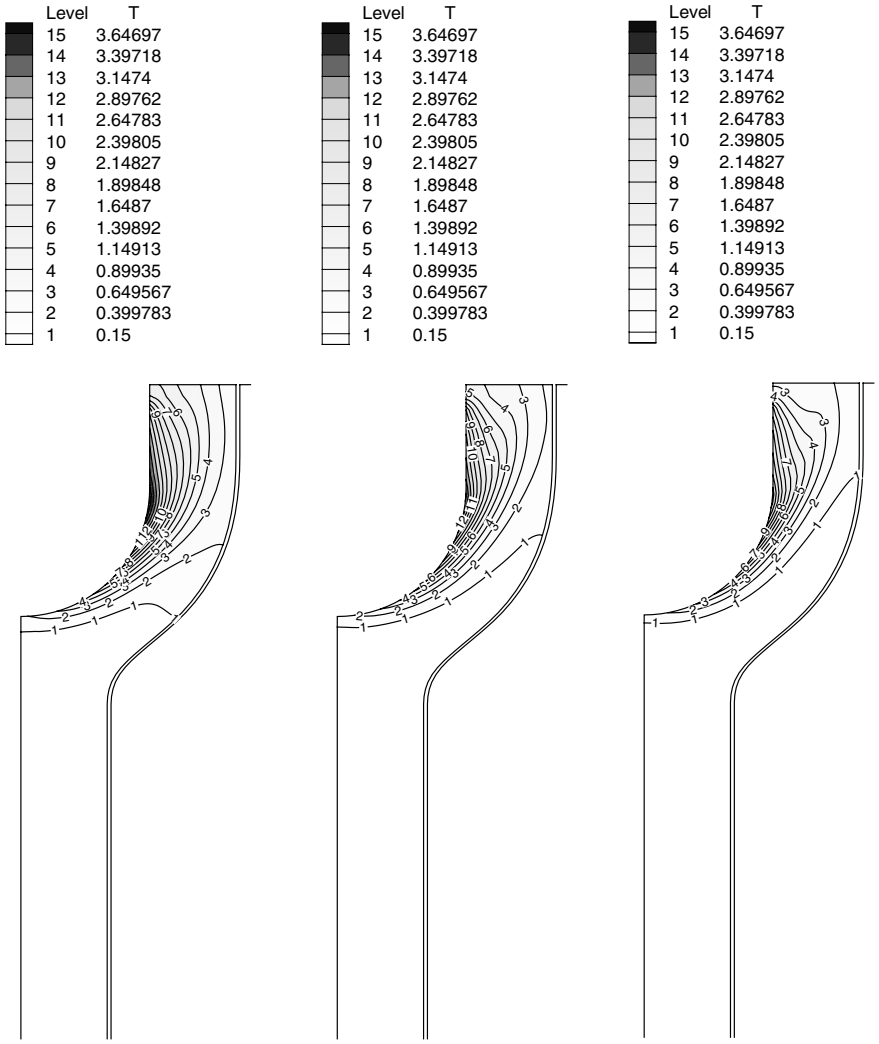

Fig. 15. Constant heat flux contours (magnified view of the window section) for (i) $Re = 500$, (ii) $Re = 700$ and (iii) $Re = 1000$.

experimental values for $Re > 600$. The reason for discrepancy is thought to be a result of the three-dimensionality of the flow for $Re > 400$ [23].

5.3. Grid independence test for ADSS geometry

The Numerical simulation has been performed for $Re = 500$ using the isothermal boundary imposed on the window of the computational domain shown in Fig. 1.

The following three meshes are considered for the grid sensitivity analysis:

(A) 33 grid points in the cross-stream direction × 271 grid points in the streamwise direction having 8943 nodes and 8640 bilinear elements.
(B) 51 grid points in the cross-stream direction × 307 grid points in the streamwise direction with 15,657 nodes and 15,300 bilinear elements.
(C) 69 grid points in the cross-stream direction × 367 grid points in the streamwise direction with 25,323 nodes and 24,888 bilinear elements.

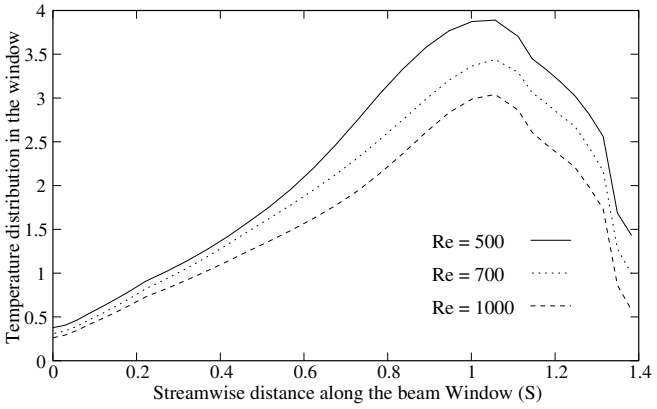

Fig. 16. Temperature distribution along the beam window for constant flux for (i) $Re = 500$, (ii) $Re = 700$ and (iii) $Re = 1000$.

As one moves from coarse grid to fine grid, the maximum deviation in the Nusselt number calculated along the beam window is found to be less than 1%. Therefore, in the present study the grid consisting of (33×271) nodes is chosen for all computations.

6. Result and discussions

6.1. Laminar flow and heat transfer characteristics

Fig. 7 shows streamlines pattern in the flow field for $Re = 500$, 700 and 1000. At $Re = 500$, a primary vortex is observed near the inlet section along the guide due to sudden expansion of the flow domain. In addition, recirculation regions are observed in the riser section starting from 180° turn all along the flow guide and also near to the exit plane along both the beam window and the flow guide. At $Re = 700$ and 1000, the size of the primary vortex decreases due to increasing velocity field and multiple vortices are created in the recirculation region in the riser section along the flow guide. The flow separation and formation of the vortices near the inlet section and close to the exit plane can be attributed to the expansion of the flow passage establishing an adverse pressure gradient therein. Near the tip of the flow guide, the fluid experiences a change (180°) in direction. The higher velocity fluid moves towards the outer wall under the influence of centrifugal force. The momentum of the fluid near the inner side (here it is the flow guide) decreases. The low momentum of the

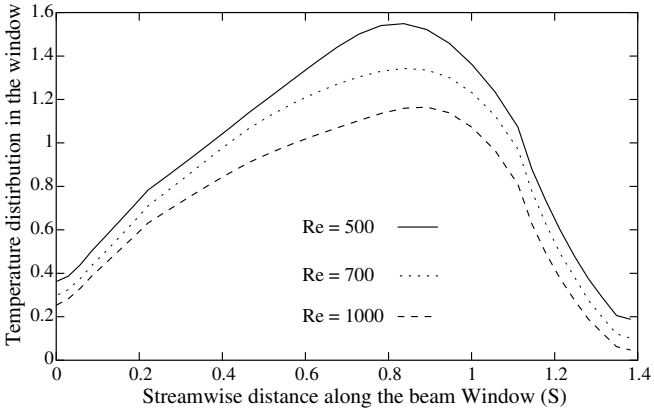

Fig. 18. Temperature distribution along the beam window for variable flux for (i) $Re = 500$, (ii) $Re = 700$ and (iii) $Re = 1000$.

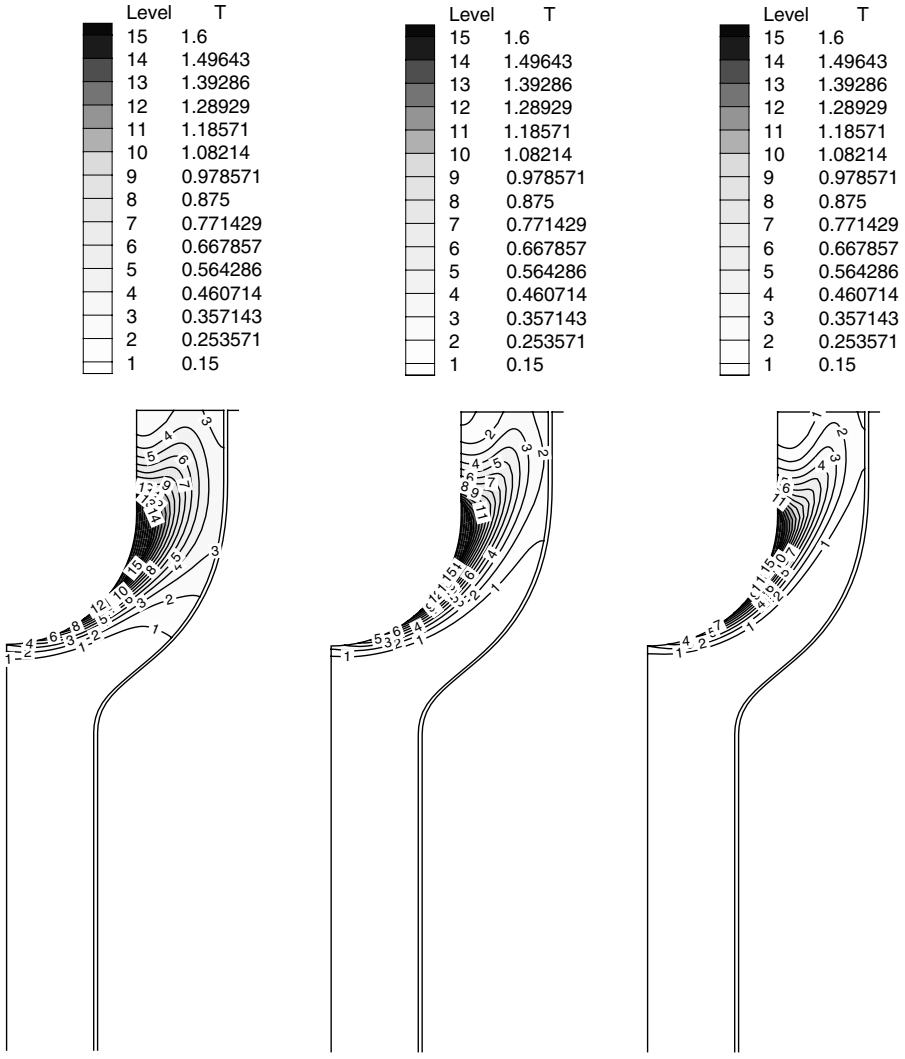

Fig. 17. Variable heat flux contours (magnified view of the window section) for (i) $Re = 500$, (ii) $Re = 700$ and (iii) $Re = 1000$.

fluid on the flow guide eventually leads to a flow separation and reversal.

For all the Reynolds numbers, pressure (Fig. 8) is seen to increase near the zone of sudden expansion immediately after the inlet. Subsequently, it decreases uniformly in the straight part of the flow passage upto the bend. The pressure drop and thereby the pressure gradient is high very close to the 180° turn. Thereafter the pressure recovers up to the concave downstream, where secondary recirculation zone occurs and finally the fluid attains the atmospheric pressure at the exit plane.

The temperature contours for the isothermal window boundary for different Reynolds numbers are shown in Fig. 9. In almost all the cases, the flow is with a developing temperature field since the liquid metal under consideration has a very low-Prandtl number (0.02) and heat transfer occurs only near the exit plane. In the case of low-Prandtl number fluids, the thermal boundary layer grows faster than the velocity boundary layer. The thermal diffusivity dominates over the molecular diffusivity. Thermal boundary layer, which is seen to manifest along the window, gets thinner with increasing Reynolds number. The energy is transported through the steeper temperature gradient.

6.1.1. Calculation of local Nusselt number, skin friction coefficient and coefficient of pressure

The local skin friction coefficient and the Nusselt number based on the inlet temperature of the stream are defined in non-dimensional form as

$$C_{f_S} = \frac{2}{Re}\frac{\partial U}{\partial n}\bigg|_{\text{along the beam window}} \quad ; \quad Nu_S = -\frac{\partial \theta}{\partial n}\bigg|_{\text{along the beam window}}$$

Here, n denotes direction normal to the beam window, S is the streamwise direction along the beam window and U denotes non-dimensional velocity tangential to the wall.

Fig. 10 compares the Nusselt number distribution based on the inlet temperature (T_∞) along the window of the target system of an ADSS for the above-mentioned Reynolds numbers. It has been observed that Nusselt number increases initially and then decreases. This is in agreement with the observed variation of the thermal boundary layer. Finally the Nusselt number increases slightly near the exit plane because of boundary layer separation and creation of a small recirculation zone entailing better mixing near the exit. The Nusselt number increase with increasing Reynolds number. Fig. 11 shows $C_f \times Re$ variation along the surface of the window. From the plots it is evident that the $C_f \times Re$ remains constant along the leading edge of the window and then decreases at the exit. The peak value of $C_f \times Re$ increases with increasing Reynolds number. Also, the spatial location of the occurrence of peak values shifts towards the leading edge of the beam window for increasing Reynolds number. These may be attributed to the combined influence of curvature effect, presence of prominent vortex and the change from free slip to no slip boundary at the leading edge of window.

Fig. 12 shows the variation of coefficient of pressure ($P - P_{in}$) in the streamwise direction along the centerline of the flow space. For all the cases, C_p reduces initially. This is due to smooth backward facing step like configuration near the inlet. Pressure is recovered partially near the bend and again it drops drastically due to 180° turn and becomes almost constant. There are some oscillations near

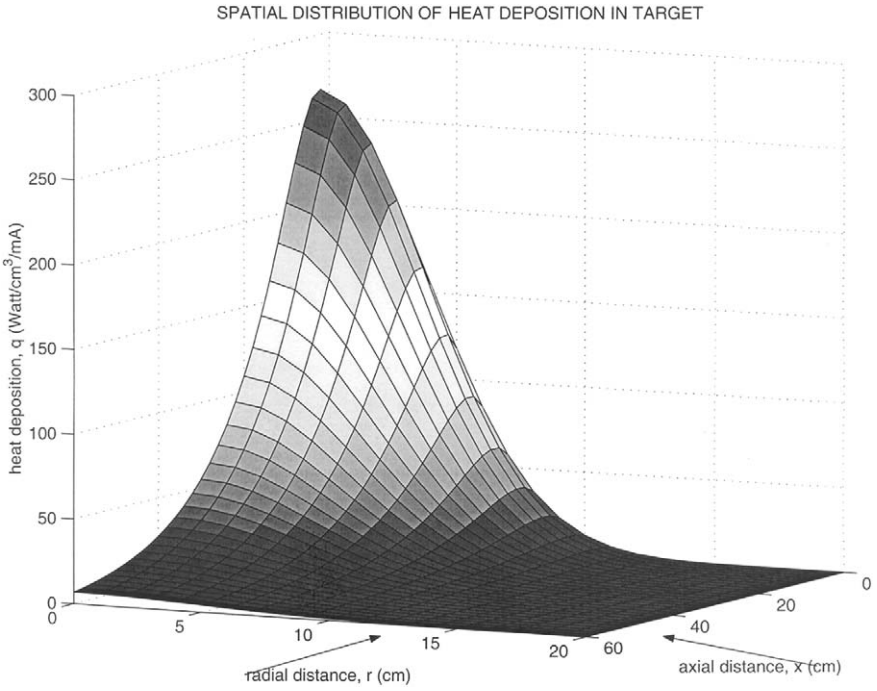

Fig. 19. Heat generation function in the liquid metal.

the exit due to the enlargement of flow area. Fig. 13 depicts the isotherms for the variable temperature along the window. A linear variation having a non-dimensional value of unity near the leading edge of the window and zero near the trailing edge is given as boundary condition. From the figure it is observed that the temperature contours gets sharper with the increase in Reynolds number and unlike the case with constant temperature it is not diffused over the curved flow space formed by the window and the flow guide. The peak value lies near the downstream of the curvature because the liquid metal convects the variable temperature. The Nusselt number plot, in the case of variable wall temperature (Fig. 14) shows an initial increase, and then it reduces all along the window. There is sharp decline in the value which is due to the curvature effect. Nusselt number increases with the increasing Reynolds number.

6.2. Constant heat flux and variable heat flux along the window

Fig. 15 shows the temperature contours along the window for constant heat flux. A non-dimensional constant heat flux value is given as the boundary condition. From the plot it is evident that the peak value occurs downstream of the curvature. The temperature contours become sharper with the increase in the Reynolds number because more heat is convected for higher Reynolds number. The value of the temperature along the window for this case is shown in Fig. 16. The peak values lies at $S = 1.0$ which is at the downstream of the window curvature. The peak value of the constant flux case is approximately 3.6 times greater than that of the constant temperature case. The temperature value along the beam window decreases with the increase in Reynolds number.

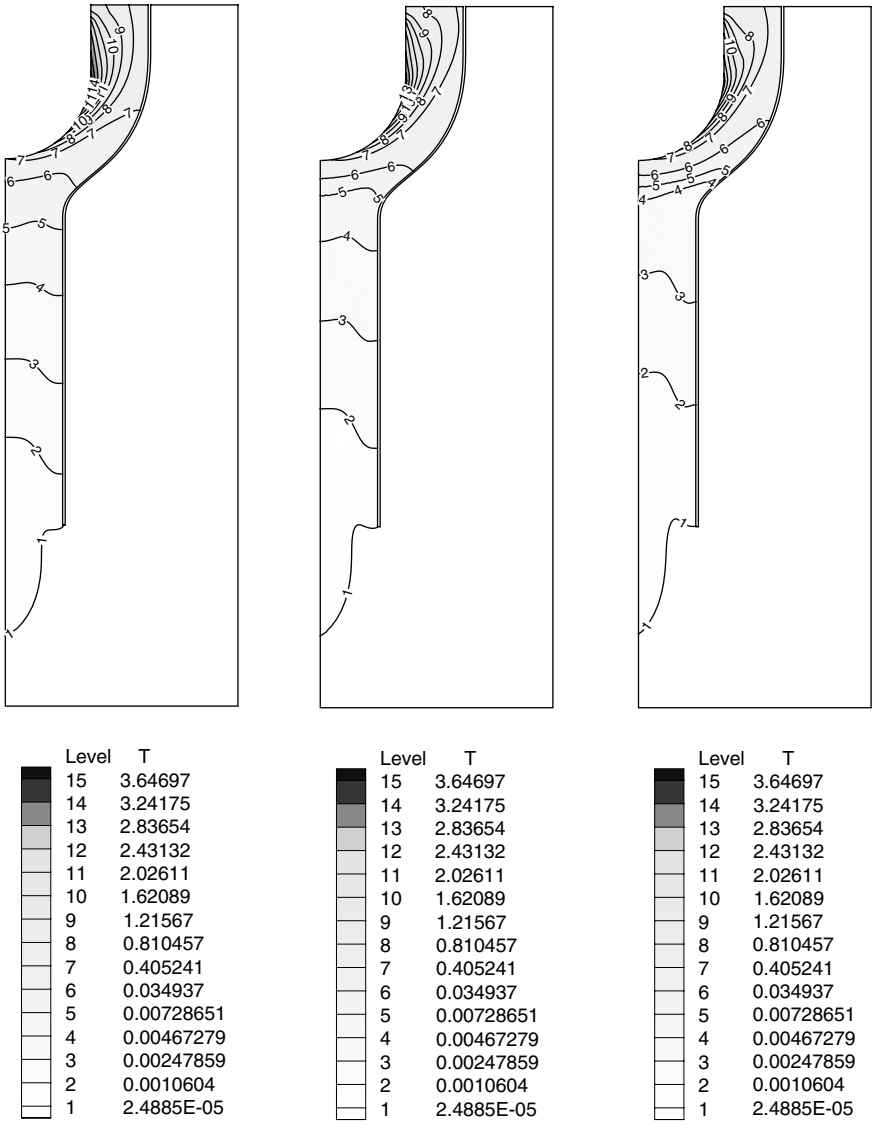

Fig. 20. Temperature contours for constant heat flux and heat generation (i) $Re = 500$, (ii) $Re = 700$ and (iii) $Re = 1000$.

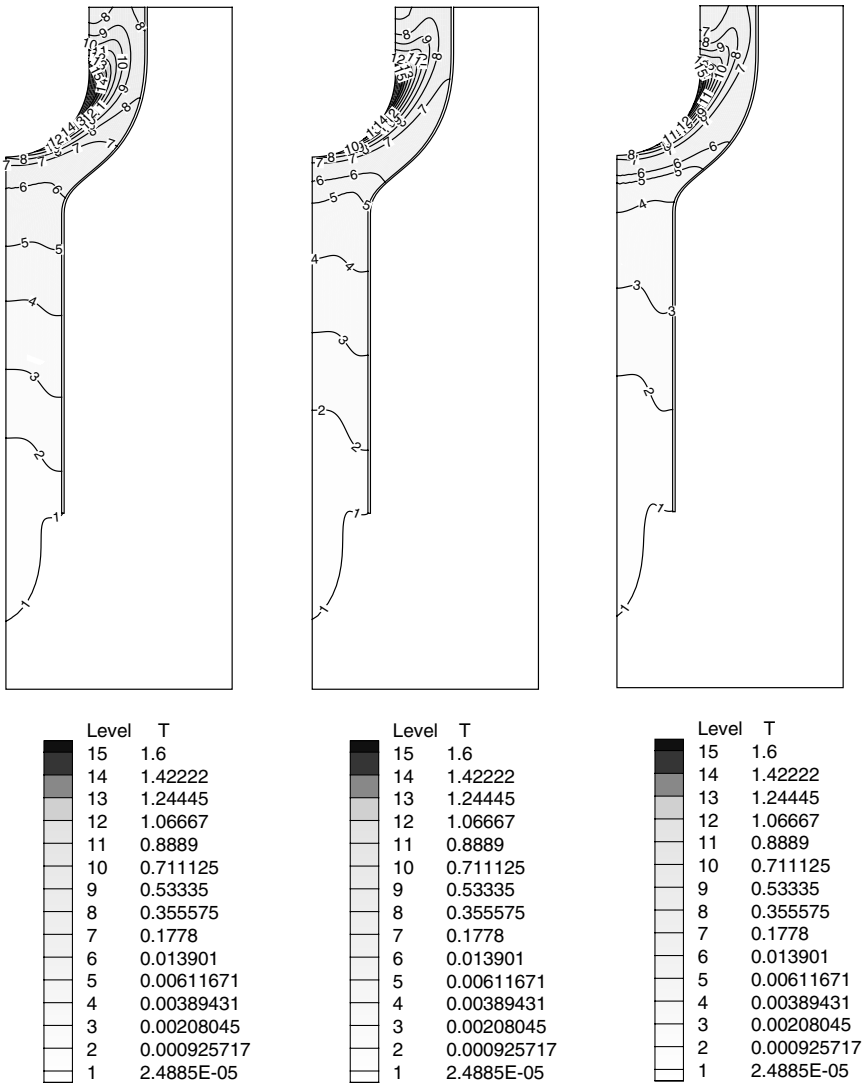

Fig. 21. Temperature contours for variable heat flux and heat generation (i) $Re = 500$, (ii) $Re = 700$ and (iii) $Re = 1000$.

Fig. 17 depicts the isotherms for the variable heat flux case. The peak value of the temperature occurs along the curved portion of the window. The peak value is about 1.6 times greater than that of the case with constant temperature window boundary. The value of the temperature along the window is shown in Fig. 18. The peak value occurs at the non-dimensional value of $S = 0.8$, which is along the window curvature.

6.3. Heat generation

Heat generation in the liquid metal was not considered so far. The liquid metal can be reactive as well. While taking cognition of the presence of heat source, heat generation function is developed for 1 GeV Proton beam based on the data obtained from FLUKA code [6]. The heat generation function is shown in Fig. 19 where the variations along the axial and radial direction are shown. Fig. 20 shows the temperature contours for the heat generation

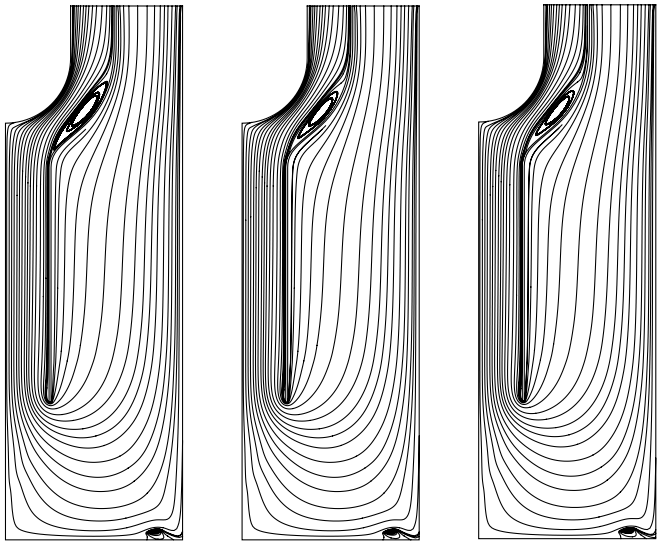

Fig. 22. Streamline plots for (a) $Re = 1.4 \times 10^5$, (b) $Re = 2.8 \times 10^5$ and (c) $Re = 5.6 \times 10^5$.

within the LBE and constant heat flux along the beam window. Fig. 21 shows the temperature contours for the heat generation within the LBE and variable heat flux along the window. Unlike for the non-reacting case, here the influence of the proton beam bombardment on the window is noticed not only in the downstream of the window but also upstream, close to the tip of the flow guide. However for the laminar case, the peak temperature value lies along the beam window.

6.4. Flow and heat transfer characteristics of turbulent flows

Figs. 22–24 show the streamlines, kinetic energy and temperature contours for three different Reynolds numbers 1.4×10^5, 2.8×10^5 and 5.6×10^5. Streamline plots shown in Fig. 22 indicate that there is a flow separation and reattachment in the convex bend along the flow guide near the exit plane and the size of the separated eddy decreases with the increase in the Reynolds number. A small vortex appears near the bottom edge of the target system. Another vortex is seen at leading edge of the return path on the flow guide. The recirculation zone starts near the 180° turn and its size decreases with increase in Reynolds number. In the case of turbulent flows, the flow curvature plays a significant role. The gradient $\frac{\partial\bar{v}}{\partial y}$ is non-zero, as is the derivative of $\bar{u}$ in x-direction. Here $\overline{v'^2}$ is produced by the mean shear. The cross-stream normal stress, $\overline{u'^2}$ develops from the pressure strain correlation. Near the leading edge of the window, the fluid experiences concave flow followed by convex flow, whereas the opposite occurs for flow near the flow guide. It has been observed for the flows with the curvature, that the quantity, $\overline{u'v'}$ first increases and then decreases in magnitude on the window, while the opposite occurs near the flow guide. Therefore, in the case of turbulent flows, the

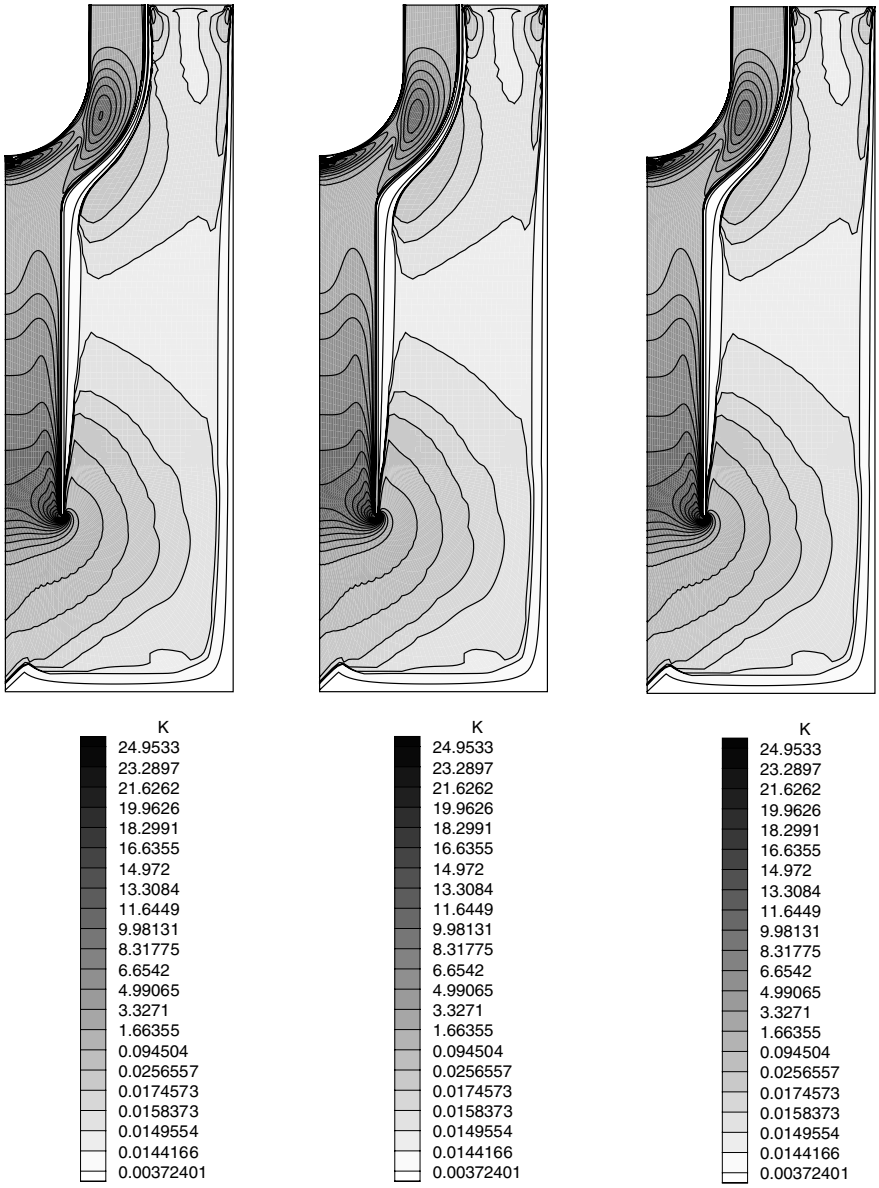

Fig. 23. Kinetic energy contours for (a) $Re = 1.4\times10^5$, (b) $Re = 2.8\times10^5$ and (c) $Re = 5.6\times10^5$.

enhanced transverse momentum transport occurs towards the inner boundary of the curved section and the separation is delayed. As a matter of fact it is prevented; in contrast to the situation that arises in laminar flow. The reason can be attributed to the presence of fluid particles with higher kinetic energy. Separated flows are observed in the concave zone of the concave region. Clearly, three Reynolds numbers give good qualitative consistency, the vortex formation appears to be well reproduced.

Fig. 23 depicts the variation of kinetic energy in the flow field. The k–ϵ model predicts the peak of the fluctuations in the immediate downstream zone of the bend. The kinetic energy increases further near the window. However, the physics of turbulence indicates that the turbulent kinetic energy stems from contributions of low frequency fluctuations. Therefore the k–ϵ model of turbulence cannot capture the exact distribution of kinetic energy. The kinetic energy gives an indication of turbulent viscosity distribution in the flow field. Fig. 24 presents the distribution of the time–mean temperature over the flow field. At the bend on the window, all the cases show convection from the wall. The temperature contours indicate that the amount of heat diffusion towards the radial direction decreases with the increase in the Reynolds number because more thermal energy is convected away from the wall by the increased velocity of LBE. The Nusselt number distribution is shown in Fig. 25. The maximum value of the Nusselt number lies downstream of the stagnation zone. The Nusselt number increases with increasing Reynolds number.

7. Conclusions

A computational study using SUPG based finite element method has been accomplished to determine the laminar and turbulent flow and heat transfer characteristics of LBE in the target module of an ADSS. The geometry has a sharp 180° turn and straight flow guide. The flow structure, pressure variation and the temperature along the beam window for different boundary conditions have been predicted numerically. In the laminar case of the target

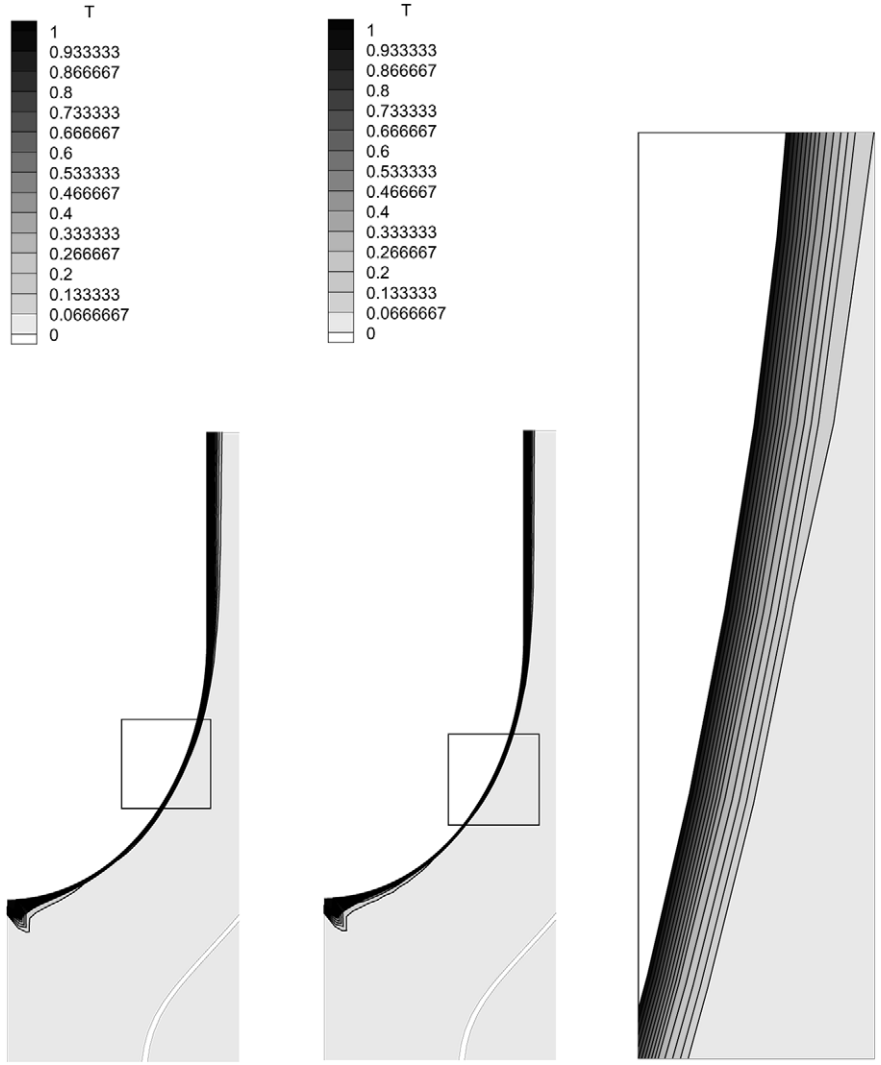

Fig. 24. Temperature contours (magnified view of the window section) for (a) $Re = 1.4 \times 10^5$, (b) $Re = 2.8 \times 10^5$ and (c) (magnified view of the rectangular portion shown in the figure (a) and (b)) for $Re = 5.6 \times 10^5$.

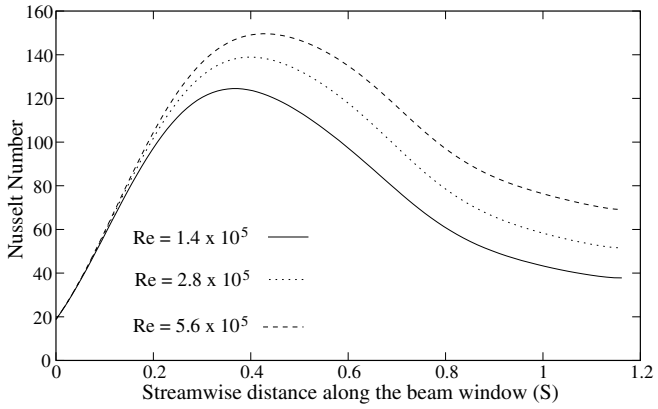

Fig. 25. Nusselt number distribution for (a) $Re = 1.4 \times 10^5$, (b) $Re = 2.8 \times 10^5$ and (c) $Re = 5.6 \times 10^5$.

system, vortices are generated at the smooth backward facing step near the inlet (primary vortex), near the 180° turn and at the exit . The size of the primary vortex in the downcomer section decreases due to increasing Reynolds number whereas the size of other vortices increases. Temperature contours with isothermal window and variable temperature boundary indicate the thermal energy diffuses towards the radial direction along the window. The diffusion decreases with the increase in the Reynolds number. The Nusselt number and the skin friction coefficient on the window surface show an overall increase for the increasing Reynolds number. This may attributed due to high mass flow rate. The temperature contours for different thermal boundary conditions are traced and the temperature distribution on the beam window is calculated. The peak value of the non-dimensional temperature for the constant flux case is nearly 2.25 times that of the variable heat flux case. The isotherms substantiate the above conclusion. The isotherms for the case of heat generation in LBE indicate the following. The thermal source is diffused upstream of the beam window and extend till the leading edge of the flow guide (180° turn). The kinetic energy contours depict the distribution of turbulent viscosity. The temperature contours indicate that the higher mass flow rate of LBE advects the total spallation heat that is generated as a consequence of the interaction of the proton beam and the LBE target system. Since there are vortices in the bottom wall of the ADSS target module, it is desirable that the shape of the flow guide be modified. There will be high probability of appearance of the hot spots in the flow space as a consequence of the creation of recirculating vortices, which is an undesirable feature in the ADSS design. It is understood that a suitable modification of the flow guide is likely to improve the thermal–hydraulics performance of the ADSS target system. Also instead of a flat bottom wall (with sharp edges), a smoother (curved) wall is expected to avoid the formation of small recirculation zone on the bottom wall. The streamlines, near the bottom wall provide the guideline for the shape optimization of the curved bottom wall.

Acknowledgment

This investigation has been sponsored by the Board of Research in Nuclear Sciences (BRNS), Grant No. 2002/34/6, India.

References

[1] C. Rubbia, J.A. Rubio, S. Buono, F. Carminati, N. Fietier, J. Galvez, C. Geles, Y. Kadi, R. Klapisch, P. Mandrillon, J.P. Revol, Ch. Roche, Conceptual design of a fast neutron operated high power energy amplifier, CERN Report, CERN-AT-95-44 (ET), Geneva, 29th September 1995.

[2] J.R. Maiorino, A.d. Santos, S.A. Pereira, The utilization of accelerators in sub critical systems for energy generation and nuclear waste transmutation—the World status and a proposal of a national R&D program, Brazil. J. Phys. 33 (2) (2002) 267–272.

[3] T.V. Dury, B.L. Smith, G.S. Bauer, Design of the European spallation source liquid–metal target using computational fluid dynamics, J. Nucl. Technol. 127 (1999) 218–232.

[4] C.H. Cho, T.Y. Song, N.I. Tak, Numerical design of a 20 MW lead–bismuth spallation target for an accelerator-driven system, Nucl. Eng. Des. 229 (2004) 317–327.

[5] A. Batta, C.H.M. Broeders, X. Cheng, A. Konobeyev, J. Neitzel, N. Tak, A. Travleev, Window target unit for the XADS lead–bismuth cooled primary system, in: Proceedings of the International Workshop on P and T and ADS Development 2003, Mol, Belgium, 6–8 October.

[6] S. Buono, Y. Kadi, C. Rubbia, Energy deposition of a Proton beam in the lead target of the energy amplifier, CERN/ET Internal note, 97-11, 1985.

[7] A.J. Chorin, A numerical method for solving incompressible viscous flow problems, J. Comput. Phys. 2 (1967) 12–26.

[8] J.N. Reddy, D.K. Gartling, The Finite Element Method in Heat Transfer and Fluid Dynamics, CRC Press, Florida, 1994.

[9] R.L. Lewis, P. Nithiarasu, K.N. Seetharamu, Fundamentals of the Finite Element Method for Heat and Fluid Flow, John Wiley and Sons, England, 2004.

[10] G. Comini, S. Del Giudice, A k–ϵ model of turbulent flow, Numer. Heat Transfer 8 (1985) 133–147.

[11] F.H. Harlow, J.E. Welch, Numerical calculation of time-dependent viscous incompressible flow of fluid with free surface, Phys. Fluids 8 (1965) 2182–2188.

[12] J. Donea, S. Giuliani, H. Laval, Finite element solutions of the unsteady Navier–Stokes equations by fractional step method, Comput. Meth. Appl. Mech. Eng. 30 (1982) 53–73.

[13] B. Ramaswamy, T.C. Jue, J.E. Akin, Semi-implicit and explicit finite element schemes for coupled fluid/thermal problems, Int. J. Numer. Meth. Eng. 34 (1992) 675–696.

[14] C.G. du Toit, Finite element solution of the Navier–Stokes equations for incompressible flow using a segregated algorithm, Comput. Meth. Appl. Mech. Eng. 151 (1998) 131–141.

[15] P.K. Maji, G. Biswas, Analysis of flow in the spiral casing using a streamline upwind Petrov Galerkin method, Int. J. Numer. Meth. Eng. 45 (1999) 147–174.

[16] A.N. Brooks, T.J.R. Hughes, Streamline upwind Petrov–Galerkin formulations for convection dominated flows with particular emphasis on the incompressible Navier Stokes equations, Comput. Meth. Appl. Mech. Eng. 32 (1980) 199–259.

[17] B.E. Launder, D.B. Spalding, The numerical computation of turbulent flows, Comput. Meth. Appl. Mech. Eng. 3 (1974) 269–289.

[18] A.C. Benim, W. Zinser, Investigation into the finite element analysis of confined turbulent flows using a k–ϵ model of turbulence, Comput. Meth. Appl. Mech. Eng. 51 (1985) 507–523.

[19] G. Biswas, V. Eswaran, Turbulent Flows: Fundamentals, Experiments and Modeling, CRC Press, 2002, pp. 319–392.

[20] U. Ghia, K.N. Ghia, C.T. Shin, High-Re solutions for incompressible flow using the Navier–Stokes equations and a multigrid method, J. Comput. Phys. 48 (1982) 387–411.
[21] B.F. Armaly, F. Durst, J.C.F. Pereira, B. Schonung, Experimental and theoretical investigation of backward-facing step flow, J. Fluid Mech. 127 (1983) 473–496.
[22] J. Kim, P. Moin, Application of fractional step method to incompressible Navier–Stokes equations, J. Comput. Phys. 59 (1985) 308–323.
[23] G. Biswas, M. Breuer, F. Durst, Backward-facing step flows for various expansion ratios at low and moderate Reynolds numbers, J. Fluids Eng. 126 (2004) 362–374.